REPORT DOCUMENTATION PAGE

Form Approved
OMB No. 0704-0188

1. REPORT DATE *(DD-MM-YYYY)*	2. REPORT TYPE	3. DATES COVERED *(From - To)*
04/01/2014	Final	03/01/2013-02/28/2014

4. TITLE AND SUBTITLE
Experimental and Theoretical Probing of Molecular Dynamics at Catalytic and Ionic Liquid Interfaces

5a. CONTRACT NUMBER

5b. GRANT NUMBER
FA9550-13-1-0094

5c. PROGRAM ELEMENT NUMBER

6. AUTHOR(S)
Stephen R. Leone
Gregory A. Voth
Hai-Lung Dai

5d. PROJECT NUMBER

5e. TASK NUMBER

5f. WORK UNIT NUMBER

7. PERFORMING ORGANIZATION NAME(S) AND ADDRESS(ES)
Regents of the University of California, University of California, Berkeley
Sponsored Projects Office
2150 Shattuck Avenue, Suite 313
Berkeley, CA 94704-5940

8. PERFORMING ORGANIZATION REPORT NUMBER

9. SPONSORING/MONITORING AGENCY NAME(S) AND ADDRESS(ES)
Dr. Michael Berman
USAF, AFRL, AFOSR
875 N. Randolph Street 11.
Suite 325, Room 3112
Arlington, VA 22203

10. SPONSOR/MONITOR'S ACRONYM(S)

11. SPONSOR/MONITOR'S REPORT NUMBER(S)

12. DISTRIBUTION/AVAILABILITY STATEMENT
Approved for public release; distribution is unlimited.

13. SUPPLEMENTARY NOTES

14. ABSTRACT
A one-year, multi-university, experimental and theoretical research program is completed, in which in-depth investigations of electron dynamics, structure and reactivity at interfaces, specifically addressing the reactivity and structure of catalytic materials, ionic liquids, and alternative fuels production. A new platform to investigate charge state dynamics at the surfaces of photocatalytic materials has been established. Femtosecond time-resolved surface photovoltage has been measured for a ZnO surface. A powerful new condensed phase reactive dynamics theoretical method known as the Fragment Molecular Orbital Multistate Reactive Molecular Dynamics (FMO-MS-RMD) has been developed and applied to obtain the reactive force field for protonated water clusters. Second Harmonic Generation from the surface of metallic nanoparticles has been detected for the first time, and the response of the second harmonic light to the change of the colloidal conditions, can be used to determine the mechanism and rates of reactions occurring at the nanoparticle surface. A method to vastly increase the two photon fluorescence yield of metallic nanoparticles, based on bonding of thiol molecules to the particle, has been discovered, a process that has implications for the use of metallic quantum dots in sensor technology and biomedical imaging. Ionic liquid interfaces have been investigated by second harmonic generation and by thermal vaporization coupled with vacuum ultraviolet mass spectrometry.

15. SUBJECT TERMS
Surface, interface, photocatalysis, fluorescence yield, ionic liquid, reactive force field

16. SECURITY CLASSIFICATION OF:			17. LIMITATION OF ABSTRACT	18. NUMBER OF PAGES	19a. NAME OF RESPONSIBLE PERSON
a. REPORT	b. ABSTRACT	c. THIS PAGE			Stephen R. Leone
Unclassified	Unclassified	Unclassified	Unclassified Unlimited	21	19b. TELEPHONE NUMBER *(Include area code)* 510-643-5467

Final Report
Experimental and Theoretical Probing of Molecular Dynamics at Catalytic and Ionic Liquid Interfaces

Stephen R. Leone (University of California, Berkeley) – Subtask I
Gregory A. Voth (University of Chicago) – Subtask II
Hai-Lung Dai (Temple University) – Subtask III
Principal Investigators

Abstract

A one-year, multi-university, experimental and theoretical research program is completed, in which in-depth investigations of electron dynamics, structure and reactivity at interfaces, specifically addressing the reactivity and structure of catalytic materials, ionic liquids, and alternative fuels production. A new platform to investigate charge state dynamics at the surfaces of photocatalytic materials has been established. Femtosecond time-resolved surface photovoltage has been measured for a ZnO surface. A powerful new condensed phase reactive dynamics theoretical method known as the Fragment Molecular Orbital Multistate Reactive Molecular Dynamics (FMO-MS-RMD) has been developed and applied to obtain the reactive force field for protonated water clusters. Second Harmonic Generation from the surface of metallic nanoparticles has been detected for the first time, and the response of the second harmonic light to the change of the colloidal conditions, can be used to determine the mechanism and rates of reactions occurring at the nanoparticle surface. A method to vastly increase the two photon fluorescence yield of metallic nanoparticles, based on bonding of thiol molecules to the particle, has been discovered, a process that has implications for the use of metallic quantum dots in sensor technology and biomedical imaging. Ionic liquid interfaces have been investigated by second harmonic generation and by thermal vaporization coupled with vacuum ultraviolet mass spectrometry.

Introduction

A multi-university program of experimental and theoretical research using spectroscopic and multiscale dynamic simulations is completed. In this program the electron dynamics, the structure and reactivity at interfaces as well as the properties of reactive interactions at the interfaces were explored. The program consisted of three subtasks. The **first subtask** utilized a newly constructed surface science apparatus in conjunction with femtosecond ultraviolet and extreme ultraviolet laser pulses to investigate the electronic structure and electron dynamics at the surface and subsurface of photocatalytic materials via photoemission spectroscopy. The investigations were focused on monitoring the charge transfer between the bulk and the surface of semiconductor materials, but also on exploring how artificially created defects change the

absorption properties and the ultrafast electron dynamics at the semiconductor surface. Furthermore, in collaboration with the Air Force scientists, the reactivity of ionic liquid molecules, especially those of interest for propulsion were investigated. The **second subtask**, in theoretical research, concerned the development and application of a powerful new condensed phase reactive dynamics method known as the Fragment Molecular Orbital Multistate Reactive Molecular Dynamics to enable efficient computer simulation of large scale reactive condensed phase systems at a high level of accuracy. In the **third subtask,** second harmonic light scattering was employed to characterize the surface of metallic nanoparticles in colloids and the interface between room temperature ionic liquids and the electrode. For the first time it has been shown that second harmonic generation from the surface of metallic nanoparticles can be detected and used to determine the mechanism and rates of reactions occurring on nanoparticles.

Subtask I

Ultrafast High Harmonic, Soft X-Ray Laser Probing Molecular Dynamics

Stephen R. Leone – University of California, Berkeley

The surface electronic properties of metal oxides are important because of their many potential applications in photochemistry and catalysis. Understanding ultrafast photoinduced processes at the surfaces of these materials is a defining principle that can guide advances in the next generation of catalysts to produce storable fuels from sustainable inputs.

A one year experimental investigation of electron dynamics at the semiconductor surfaces is completed. The goals of this work are (i) to investigate the charged carrier dynamics at the surface of semiconductors that can be used to produce storable fuels from sustainable inputs using visible light and (ii) to tune the electronic structure of those semiconductors to absorb visible light. This report summarizes the first results obtained on electron dynamics at the surface of a single crystal zinc oxide using a newly constructed experimental setup. Zinc oxide can be used in different compounds such as ZnO-GaN[1] and ZnO-CdS,[2, 3] which are promising photocatalysts for hydrogen production via photocatalytic water splitting.

1. Experimental

The new experimental setup consists of two main parts (i) the femtosecond (fs) laser system in conjunction with the pump-probe setup as well as the high order harmonics generation (HHG) system, and (ii) an ultra-high vacuum (UHV) surface science chamber. Figure 1 shows a schematic representation and a picture of the HHG setup together with the UHV chamber. Briefly, the femtosecond laser light is produced with a Ti:sapphire oscillator (KMLabs) continuously pumped by a 6 W Spectra Physics Millennia Nd:YVO_4 laser. The laser pulses are amplified with a Nd:YLF laser pumped Ti:sapphire amplifier (Dragon, KMLabs) to yield 30 fs pulses with a typical power of 2.2 W at a repetition rate of 1 kHz. For these investigations femtosecond laser pulses at a central wavelength of 800 nm, 400 nm, and 266 nm as well as femtosecond laser pulses in the XUV spectral domain are used. The laser pulses at 400 nm and 266 nm are generated by frequency doubling or tripling of the fundamental wavelength in a homebuilt third harmonic generator using BBO crystals. The fs XUV pulses are produced via HHG in rare gases. For the HHG process, the laser beam at the central wavelength of 800 nm is focused to 10^{14}-10^{15} W cm^{-2} in a high density of a rare gas i.e. Ar for the efficient production of low energy harmonics up to 42 eV and Ne for the efficient production of higher energy harmonics up to 100 eV. In order to obtain monochromatic fs soft-x ray pulses, the HH beam is dispersed by a plane grating in first order diffraction at grazing incidence. Subsequently the HH beam is focused on the sample surface inside of the UHV chamber by cylindrical and toroidal mirrors to a spot size of about 0.2 mm. A slit mounted at the entrance in the UHV chamber allows a single harmonic to enter the UHV chamber and stops all the other wavelengths. This

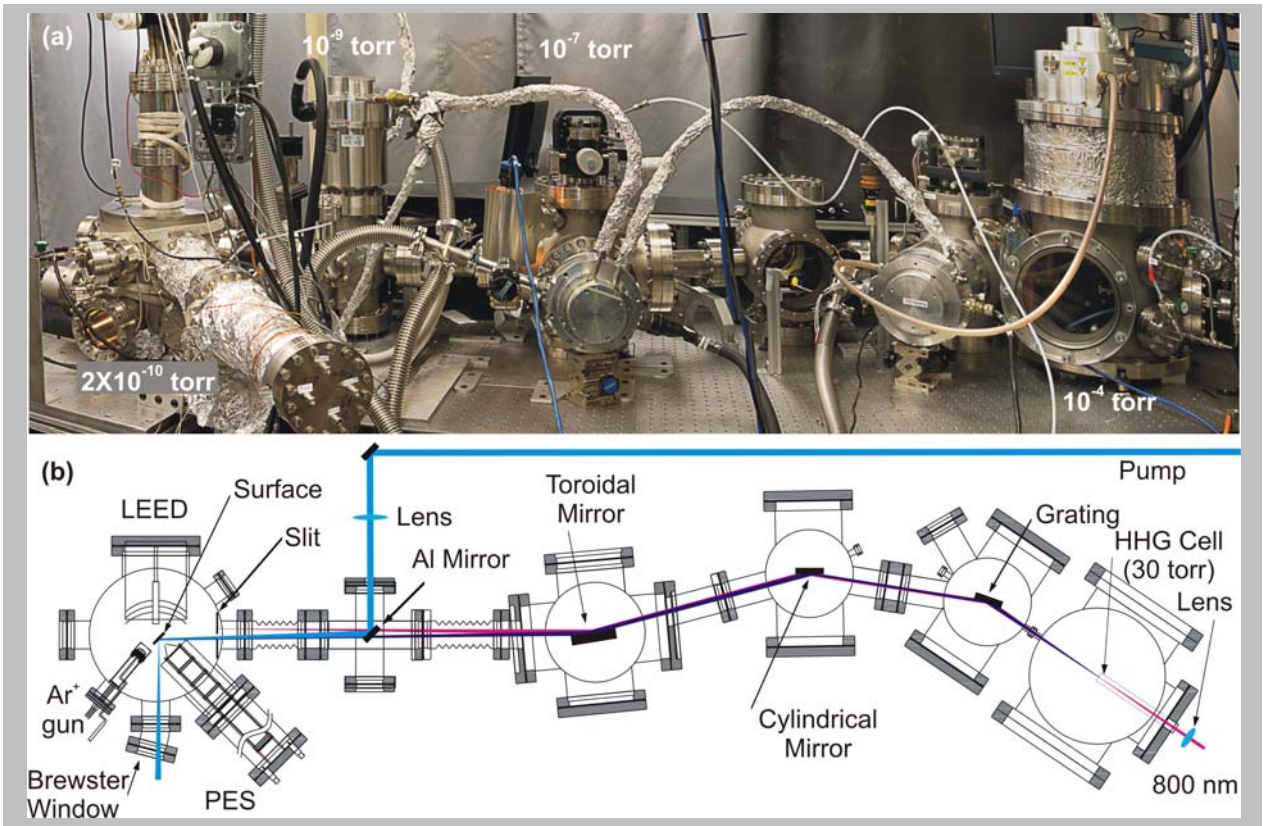

Fig. 1 (a) Photograph and (b) Schematic layout of the fs-soft x-ray source together with the UHV surface science chamber.

slit also allows an efficient differential pumping of the vacuum apparatus. An aluminum mirror installed inside of the vacuum apparatus a few millimeters above the XUV laser beam is used to steer the pump into the UHV chamber and to ensure the overlap between the pump and the probe beams onto the sample surface (cf. Figure 1).

The UHV surface science chamber contains specific tools for surface preparation and characterization arranged on two levels. The upper level of the surface science chamber is equipped with a homebuilt time-of-flight photoelectron spectrometer (PES) to investigate the electron dynamics at the surface of photocatalytic materials, a commercial low energy electron diffraction (LEED) instrument to study the surface crystallinity, and a home built Ar ion gun for surface cleaning. The upper level of the surface science chamber is schematically represented in Figure 1. The lowest level hosts an Auger electron spectrometer to investigate the surface composition and cleanliness, an ion gauge to measure the vacuum pressure, a gas inlet as well as a home built evaporator. The surface sample is attached to a liquid nitrogen cryostat and it is mounted in the center of the UHV chamber. The surface sample-cryostat assembly can be vertically translated to both vacuum chamber levels and horizontally rotated by 360° by a mechanical manipulator. Furthermore, a xy-horizontal translation stage allows a movement of the assembly by ±12 mm from the midpoint. The crystal position can be reproduced with better than 0.02 mm and 0.5° accuracy.

The sample surface can be cooled down to 100 K and resistively heated up to 1200 K. During the experiments a pressure of about 2×10^{-10} Torr in achieved in the surface science chamber by means of a multiple differential pumping stages. The obtained pressures in the vacuum chambers are shown in Figure 1.

The photoelectron spectra are measured by means of a home built TOF-PES consisting of a 1 m long, double wall mu-metal tube. Electron detection is accomplished by a microchannel-plate amplifier in conjunction with a 5 GHz multichannel scaler electronics unit (FAST P7889) for data acquisition. The sample surface is positioned 5 mm away from the PES entrance with the surface normal parallel to the spectrometer axis. A bias of typically 5-10 V is applied to the surface in order to prevent cutting off the low energy electrons due to the work function difference between the substrate and the spectrometer. The laser beam incidence angle is 45°. In order to avoid spectral broadening due to space charge effects, the laser intensity is carefully adjusted and the count rate is kept at small values.

For the present investigations a Ga-doped ZnO crystal (10mmx10mmx0.5mm) oriented in the [0001] direction from MTI Corp is used. The clean defect-poor ZnO(0001) surface is prepared by several cycles of Ar^+ sputtering (0.8KeV, 2μA) for 20 min followed by 30 min of annealing at 850 K in oxygen atmosphere ($P_{O_2} = 5 \times 10^{-7}$Torr). The ZnO(0001) surface cleanliness is verified by AES.

2. Electron dynamics at the surface and subsurface of ZnO(0001)

To monitor the electronic structure and the electron dynamics at the surface and subsurface of ZnO(0001), photoemission experiments are performed employing fs laser pulses at the central wavelengths of 800 nm and 266 nm. The electrons emitted at these excitation wavelengths have a kinetic energy ranging from zero to a few eV and therefore their penetration depth of multiple atomic layers can reveal insights not only about the electronic structure of the surface but also about the subsurface.

Figure 2(a) shows two photoelectron spectra, one recorded from a clean, defect poor ZnO(0001) surface and one recorded from the same surface after a 60 min of Ar^+ sputtering (I_{Ar} = 2 μA), assumed to be defect rich. The photoelectron spectra in Figure 2(a) are recorded at an excitation wavelength of 266 nm (4.66 eV) and are displayed on the kinetic energy scale. The onset of the kinetic energy scale (E_{kin} = 0 eV) is set to the half-maximum of the lowest-energy edge of the defect poor spectrum.[4, 5]

Here just the major differences between the two spectra shown in Figure 2(a) are analyzed and discussed. After Ar^+ sputtering, the width of the photoemission spectrum increases from 1.4 eV to 2.62 eV, and also an apparent increase of the photoemission intensity is observed. Laser power dependence measurements are performed to obtain more information about the photoemission changes induced by the Ar^+ sputtering process.

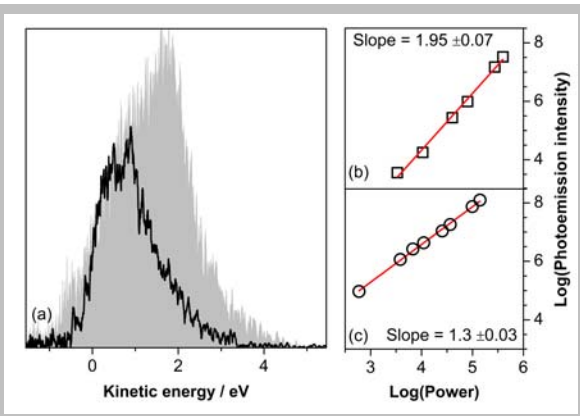

Figure 2. (a) Photoemission spectra obtained at an excitation wavelength of 266 nm from defect poor ZnO(0001) surfaces (solid line) and from a defect rich ZnO(0001) surface that is sputtered by Ar^+ ions for 60 min, I_{Ar} = 2 µA (filled spectrum). Laser power dependence of the photoemission intensities obtained at an excitation wavelength of 266 nm from the ZnO(0001) surface (b) before and (c) after 60 min Ar^+ sputtering.

Figure 2(b-c) displays in a double logarithmic representation the laser power dependence of the photoemission intensities obtained at an excitation wavelength of 266 nm from the ZnO(0001) surface before and after 60 min of Ar^+ sputtering. As displayed in Figure 2(b), two photons (slope n = 1.95 ±0.07) are required to produce the photoemission from the clean, defect poor surface. This result is in a agreement with previous photoemission investigations of defect poor ZnO surfaces, which show that the valence band maximum (VBM) is located around 7.5 eV below the vacuum energy level (E_{VAC}).[6 7]

The power dependence recorded after the Ar^+ sputtering process shows a slope of n = 1.30 ±0.03. A potential interpretation of this result might consider two mechanisms contributing to this photoemission signal: (i) a two-photon photoemission of electrons originating from the occupied electronic states below the VBM, and (ii) a single-photon photoemission process originating from defect states created by Ar^+ sputtering. Consequently, the broadening of the photoemission spectrum observed after the Ar^+ sputtering process (cf. Figure 2(a)) can be attributed to the photoemission from the newly created defect states in the band gap of ZnO(0001). The apparent increase of the photoemission intensity after Ar^+ sputtering is attributed to the single-photon photoemission of electrons from these occupied states created in the semiconductor band gap that have a higher excitation cross section than the states below the VBM, which can be accessed just by means of two-photon excitation. Occupied electronic states created by Ar^+ sputtering have been observed and reported for different metal oxides surfaces such as TiO_2[5] and Al_2O_3[8] and are attributed to oxygen vacancies at the material surface and subsurface.

A pump-probe photoemission experiment is performed to further explore the defect states created in the band gap of ZnO(0001) and their influence on the electron dynamics at the semiconductor surface. Figure 3 displays the two-color photoemission transients signals recorded by integrating the photoemission spectra from a defect poor, a defect rich, and from a defect rich ZnO(0001) surface that is annealed at 700 K in oxygen atmosphere of $5x10^{-7}$ Torr O_2. The defect rich surface is prepared by Ar^+ sputtering a defect poor surface for 60 min, I_{Ar} = 2 µA. The transients were recorded employing the wavelengths of 800 nm (1.55 eV) and 266 nm (4.66 eV), respectively. At negative time delay, the intermediate states are populated by the 266 nm laser pulses. Subsequently these states are probed by the 800 nm laser pulses. At

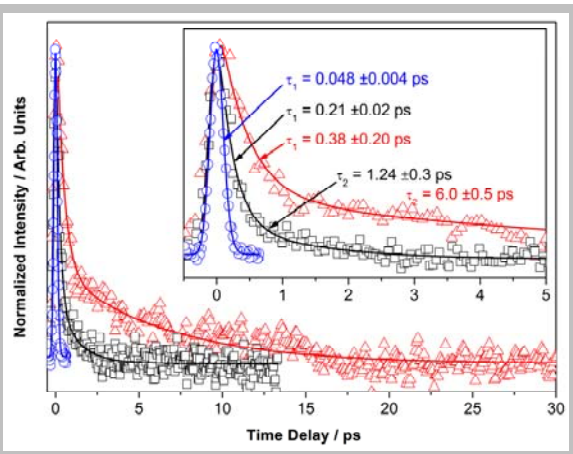

Figure 3. Two color transients signals recorded by monitoring the integral photoemission intensity as a function of the pump-probe time delay from a defect poor (open circles), defect rich (triangles), and from a defect rich ZnO(0001) surface annealed for 40 min, at 700 K in an oxygen atmosphere of $5x10^{-7}$ Torr (squares). The transients were recorded employing the pump-probe wavelengths of 800 nm and 266 nm, respectively. The blue solid line represents the best fit of a single exponential decay function convoluted by the pump-probe cross correlation function. The black and red solid lines represent the best fit to the experimental data by a second-order exponential decay function convoluted with the Gaussian autocorrelation function. Inset: Detailed view of the -0.5 ps to 5 ps pump-probe time delay region.

positive time delay the sequence of the laser pulses is exchanged (800 nm pump and 266 nm probe).

The transient obtained from the defect poor ZnO(0001) surface (open circles in Figure 3) has a symmetric peak shape centered at 0 fs time delay. The blue solid line in Figure 3 represents the best fit to the measured data by a single exponential decay function convoluted by the pump-probe cross correlation function (pulse duration 140 fs). The decay time constant obtained for the defect poor ZnO(0001) is 0.048 ±0.004 fs. After generation of defects by Ar^+ sputtering the photoemission transient signal does not change at negative time delay. However, at positive time delay this transient signal decays in 1 ps to about one third of its maximum intensity achieved at 0 fs and subsequently decays further with a slower rate. The red solid line in Figure 3 represents the best fit to the measured data obtained from the defect rich ZnO(0001) surface by a second order exponential decay function convoluted by the pump-probe cross correlation function. The time constants obtained from the fit are $\tau_1 = 0.38 \pm 0.20$ ps for the fast decay and $\tau_2 = 6 \pm 0.5$ ps for the slow decay. A transient is also recorded from the defect rich ZnO(0001) surface that is annealed for 40 min at 700 K in an oxygen atmosphere of $5x10^{-7}$ Torr O_2 (open squares in Figure 3). This transient signal resembles the main features of the transient signal obtained from the defect rich ZnO(0001) surface, but it has much faster decay rates, i.e. $\tau_1 = 0.21 \pm 0.02$ ps for the fast decay and $\tau_2 = 1.24 \pm 0.3$ ps for the slow decay.

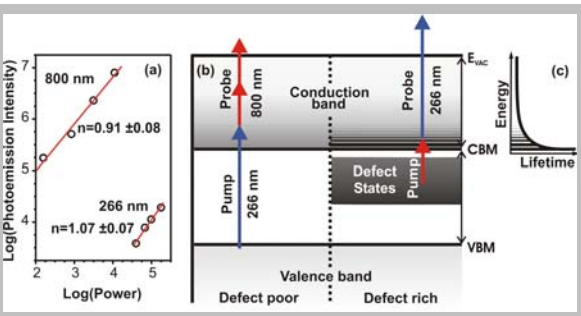

Figure 4. (a) Dependence of the photoemission intensity on the pump and probe laser power measured at a positive pump-probe delay time of 200 fs. (b) Schematic energy level diagram illustrating the assignment of the different excitation processes for a defect poor and a defect rich ZnO(0001) surface that lead to the observed transient signals in Fig. 2. (c) Shematic representation of the life time of the electronic states located in the conduction band of ZnO (adapted from Ref.6).

In the case of defect free ZnO surface the lowest photon energy of 1.55 eV (800 nm) is neither sufficient for a single nor for a two photon excitation of the electrons from the valence band into the conduction band, because the band gap of ZnO is 3.4 eV wide. Therefore, the transient photoelectron signal

obtained from the defect poor ZnO(0001) shown in Figure 3 might be attributed to a single-photon excitation at 266 nm (4.66 eV) of the electrons from the valence band into the conduction band, followed by a two photon photoemission at 800 nm. This process is schematically represented in Figure 4(b).

In order to decipher the pump-probe mechanism responsible for the transient photoemission signal recorded from the defect rich ZnO(0001) surface displayed in Figure 3, pump and probe power dependence measurements are performed. Figure 4(a) shows the dependence of the photoelectron intensity on the pump and probe laser power at a pump-probe time delay of +200 fs. As observed in the static photoemission spectra in Figure 2(a) and confirmed by the additional power dependence measurements in Figure 2(c) and Figure 4(a), the Ar^+ sputtering process creates occupied electronic states in the band gap of ZnO(0001). From these occupied states a single 800 nm pump photon (slope $n = 0.91 \pm 0.08$ in Figure 4(a)) is sufficient to excite an electron on an intermediate electronic state in the conduction band. Subsequently, a single 266 nm photon (slope $n = 1.07 \pm 0.07$ in Figure 4(a)) further excites the electrons from the intermediate states above the E_{VAC}, and consequently it probes the lifetime of the electronic states in the conduction band. This pump-probe mechanism is schematically represented in Figure 4(b).

Based on the static photoemission spectra and laser power dependence measurements presented above, the transient photoemission signal recorded from defect rich ZnO(0001) surface displayed in Figure 3 can be tentatively explained as follows. The highest photoemission intensity is reached when both the pump and the probe pulses are perfectly overlapped in time (0 fs). The fast decay measured at positive time delays with a time constant of 0.38 ± 0.20 fs might be attributed to electron decay from the initially excited intermediate states close to conduction band minimum (CBM). The lifetime of the excited states in the vicinity of the CBM increases exponentially with decreasing energy as schematically represented in Figure 4(c)[6]. The slow decay measured from defect rich ZnO(0001) with a time constant of $\tau_2 = 6 \pm 0.5$ ps might be attributed either to electron hole recombination through the defect states or to the life time of trapping states produced by Ar^+ sputtering.

The time constants obtained from the transient signal recorded on the defect rich ZnO(0001) surface (cf. Figure 4) does not change significantly if the surface is exposed to oxygen or if the surface is annealed in UHV conditions (10^{-10} Torr). However, annealing a defect rich ZnO(0001) surface at 700 K in O_2 atmosphere does cause a decrease of the decay time constants (cf. Figure 3 - open squares transient signal). The time constants obtained in this case have values between the values obtained on the defect poor and defect rich ZnO(0001) surfaces (cf. Figure 3). This experiment suggests that the defects created by Ar^+ ion sputtering consist of oxygen vacancies in the ZnO(0001) subsurface, as mentioned above and observed on different metal oxides surfaces sputtered by Ar^+ ions.[5, 8] Because these defect states created in the semiconductor subsurface are thermally stable and can lower the photon energy required for

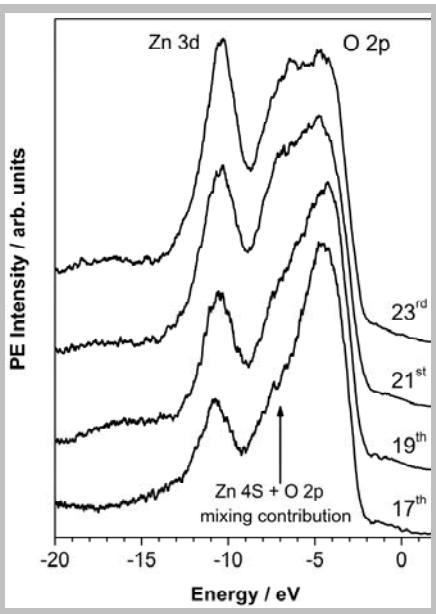

Figure 5. Normal photoemission spectra recorded from a n-type doped ZnO(0001) surface using the 17th, 19th, 21st, and 23rd harmonics of the fundamental wavelength (800 nm) of the Ti:Sapphire femtosecond laser.

photoexcitation, they can be used to tune the electronic structure of the photocatalytic materials to absorb visible light.

3. Femtosecond Soft X-ray Probing of Electron Dynamics at ZnO(0001) surface

Using femtosecond XUV pulses in conjunction with electron photoemission spectroscopy, the real time investigation of the electronic levels that gives information about the chemical bonding, the charge localization at the surface, and the charge transfer between an adsorbate and the substrate surface can be performed. Moreover, the 10 eV to 80 eV photoelectrons have an extremely low mean free path in solids,[9] which ensures a very high surface sensitivity. Here are presented some of the first preliminary results, obtained using fs-XUV laser pulses in conjunction with the new surface science chamber in which the ZnO(0001) charge transfer between the bulk and the surface is investigated.

Figure 5 shows a series of photoemission spectra recorded from ZnO(0001) at different excitation wavelengths in the XUV domain. The binding energies are referred to the Fermi level ($E_F = 0$). To determine the E_F of the ZnO(0001) sample a photoemission spectrum from a polycrystalline Mo surface that is in electrical contact with the ZnO(0001) sample is measured. The spectra display different features characteristic of a ZnO surface. The photoemission peak at −4.5 eV is due to the O 2p orbitals, while the shoulder at −7.5 eV is assigned to the Zn 4s-O 2p mixing states. The peak at −10.5 eV is due to Zn 3d states. As can be seen in Figure 5, the relative intensities of the photoemission features change as a function of the photon excitation wavelength, because the photoemission cross section of the states studied here varies with the photon excitation wavelength.

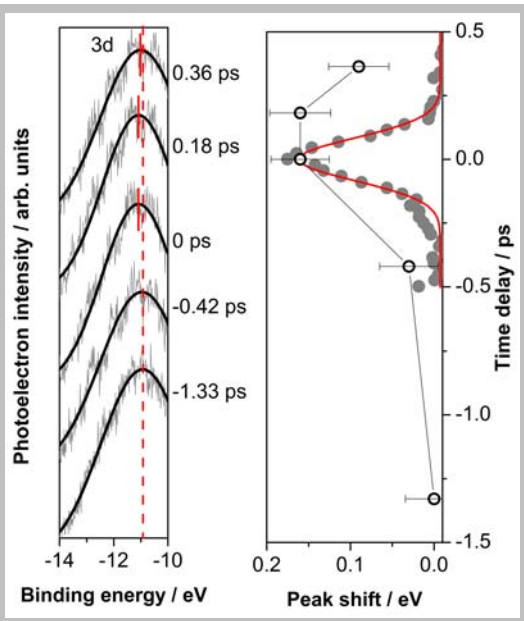

Figure 6. (left) The Zn 3d peak monitored as a function of the pump-probe delay time. The gray lines represent the measured data, while the black solid lines represent the best fit by a Gaussian function to the measured data. The long vertical dashed line is located in the center of the Zn 3d peak recorded at -1.33 ps time delay. (right) The relative energy shift of the Zn 3d peak relative to the peak recorded at -1.33 ps time delay.

In Figure 6 the photoinduced ultrafast charge transfer between the bulk and the surface of a defect poor n-type doped ZnO(1000) semi-conductor is investigated by monitoring the

transient surface photovoltage by pump-probe photoemission spectroscopy employing fs-XUV pulses. The electrons are excited from the valence band into the conduction band of the ZnO by the pump laser pulse at a central wavelength of 266 nm. Subsequently, the Zn 3d peak is monitored by the probe laser pulse (23rd harmonic of the fundamental wavelength) as a function of the pump-probe time delay. Because the ZnO crystal is n-type doped and because of the space-charge region in the vicinity of the semiconductor surface, the holes are accelerated toward the surface and the electrons toward the bulk. Consequently, a transient change of the surface photovoltage occurs, which induces a transient shift of the Zn 3d peak. The transient shift to higher binding energy of the Zn 3d photoemission peak at early pump-probe time delay with a magnitude of 0.16 eV is attributed to transport of the positively charged carrier from the bulk to the surface. Upon increasing the pump-probe time delay, a restoration of the Zn 3d peak is observed, which corresponds to the recombination of the positive and negative carriers.

The result displayed in Figure 6 is preliminary, but it demonstrates how this technique is used to track the charge carrier transport between the bulk and surface. Further investigations will be focused on monitoring the ultrafast transient change of the oxidation state of co-catalyst particles deposited on semiconductor photocatalytic surfaces as a function of co-catalyst particle size and composition. These experiments will provide information about charge transfer to the co-catalyst, charge trapping at the co-catalyst, and charge relaxation to the semiconductor surface and will allow measuring and controlling the properties of these photocatalytic systems.

4. Thermal Decomposition of Ionic Liquids

Together with Air Force Research Laboratory scientists, Steven Chambreau and Ghanshyam Vaghjiani, experiments were performed to study the thermal decomposition properties of ionic liquids. Due to the unusually high heats of vaporization of room-temperature ionic liquids (RTILs), volatilization of RTILs through thermal decomposition and vaporization of the decomposition products can be significant. Upon heating of these RTILs in vacuum, their gaseous products were detected experimentally via tunable vacuum ultraviolet photoionization mass spectrometry performed at the Chemical Dynamics Beamline 9.0.2 at the Advanced Light Source. Experimental evidence for di- and tri-alkylimidazolium cations and nitrile-containing anions indicates thermal decomposition occurs through two pathways: deprotonation of the cation by the anion, and dealkylation of the imidazolium cation by the anion. Additional evidence supporting these mechanisms was obtained using thermal gravimetric analysis/mass spectrometry, gas chromatography/mass spectrometry and temperature-jump infrared spectroscopy. In order to predict the overall thermal stability in these ionic liquids, the ability to accurately calculate both the basicity of the anions and their nucleophilicity in the ionic liquid is critical. Both gas phase and condensed phase (polarizable continuum model) density functional theory calculations provide support for the decomposition mechanisms and a means to determine thermal stabilities for ionic liquids in general.

References (Leone)

1. K. Maeda, K. Teramura, D. Lu, T. Takata, N. Saito, Y. Inoue, K. Domen, *Nature*, **2006**, 440, 295-295.
2. X. Wang, G. Liu, G. Q. Lu, H.-M. Cheng, *Int. J. of Hydrogen Energ.*, **2010**, 35, 8199-8205.
3. F. Xu, Y. Yuan, H. Han, D. Wu, Z. Gao, K. Jiang, *CrystEngComm*, **2012**, 14, 3615-3622.
4. M. E. Vaida, T. Gleitsmann, R. Tchitnga, T. M. Bernhardt, *J. Phys. Chem. C*, **2009**, 113, 10264-10268.
5. K. Onda, B. Li, H. Petek, *Phys. Rev. B*, **2004**, 70, 045415.
6. W. A. Tisdale, M. Muntwiler, D. J. Norris, E. S. Aydil, X. Y. Zhu, *J. of Phys. Chem. C*, **2008**, 112, 14682-14692.
7. S. Noothongkaew, R. Supruangnet, W. Meevasana, H. Nakajima, S. Limpijumnong, P. Songsiriritthigul, *Appl Surf Sci*, **2009**, 256, 980-983.
8. C. Niu, K. Shepherd, D. Martini, J. Tong, J. A. Kelber, D. R. Jennison, A. Bogicevic, *Surf. Sci.*, **2000**, 465, 163-176.
9. M. P. Seah, W. A. Dench, *Surf. Interf. Anal.* , **1979**, 1, 2.

Publications acknowledging AFOSR support during the last three years (Leone):

- C. J. Koh, C. L. Liu, C. Harmon, D. Strasser, A. Golan, O. Kostko, S. D. Chambreau, G. L. Vaghjiani, and S. R. Leone, *Soft ionization of thermally evaporated hypergolic ionic liquid aerosols*, *J. Phys. Chem*. **2011**, 115, 4630.

- S. D. Chambreau, J. A. Boatz, G. L. Vaghjiani, C. Koh, O. Kostko, A. Golan, and S. R. Leone *Thermal decomposition mechanism of 1-ethyl-3-methylimidazolium bromide ionic liquid*, J. Phys. Chem. (A: A. R. Ravishankara Festschrift), **2012**, 116, 5867.

- C. J. Koh, and S. R. Leone *Simultaneous ion-pair photodissociation and dissociative ionization of an ionic liquid: velocity map imaging of vacuum-ultraviolet-excited 1-ethyl-3-methylimidazolium bis(trifluoromethylsulfonyl)imide*, Mol. Phys., **2012**, 110, 1705.

- S. D. Chambreau, G. L. Vaghjiani, C. J. Koh, A. Golan, S. R. Leone, *Ultraviolet Photoionization Efficiency of the Vaporized Ionic Liquid 1-Butyl-3-methylimidazolium Tricyanomethanide: Direct Detection of the Intact Ion Pair*, J. Phys. Chem. Lett., **2012**, 3, 2910.

- M. E. Vaida, S. R. Leone, Tracing dissociation dynamics of CH_3Br in the $^3Q_0$ state with femtosecond extreme ultraviolet ionization, *Chem. Phys*. **2014,** http://dx.doi.org/10.1016 /j.chemphys.2014.01.015

- S. D. Chambreau, A. C. Schenk, A. J. Sheppard, G. R. Yandek, G. L. Vaghjiani, John Maciejewski, C. J. Koh, A. Golan, S. R. Leone, *Ultrafast excited state dynamics of an imidazolium based ionic liquid*, *J. Am. Chem. Phys.* **2014** submitted

- C. J. Koh, D. M. Popolan-Vaida, A. Golan, S. D. Chambreau, G. Vaghjiani, S. R. Leone, *Identification of reaction intermediates: hypergolic reaction of an ionic liquid with nitric acid*, (to be submitted).

Subtask II
Theory of Catalysts for Alternative Fuel

Gregory A. Voth – University of Chicago

This project in the Voth group concerned the development and application of a powerful new condensed phase reactive dynamics method known as the Fragment Molecular Orbital Multistate Reactive Molecular Dynamics (FMO-MS-RMD).[1] The methodological origins for the project are the Fragment Molecular Orbital (FMO) method and the Multistate Empirical Valence Bond (MS-EVB) force fields. In the FMO method,[2] a full electronic structure calculation of a molecular system is approximated through some combination of relatively smaller, more feasible electronic structure calculations on subsets of the molecular system. This reduces the computational cost of *ab initio* quantum chemistry calculations but also introduces a nonuniqueness issue meaning that a given molecular system does not always have one specific fragmentation. In MS-EVB,[3] a reactive molecular system is represented by some linear combination of multiple states, each state having a different bonding topology. These states form a basis set, and molecular dynamics[4] can be propagated with MS-EVB by determining the basis of states on-the-fly at each timestep.

Given a molecular system, the overall quantum mechanical (QM) molecular energy can be approximated by the many-body expansion

$$E^{\mathrm{FMO}} = \sum_{I}^{N_{\mathrm{frag}}} E_I + \sum_{I<J}^{N_{\mathrm{frag}}} (E_{IJ} - E_I - E_J) \qquad (1)$$

Here E_I is the QM energy of the Ith molecule and E_{IJ} is the QM energy of the dimer consisting of the Ith and Jth molecules. These energies–and if the derivative with respect to the atomic positions is taken, the gradients–can be efficiently calculated with highly accurate QM methods. Higher order expansions (trimers, tetramers, etc.) can be included with additional computational cost but it has been shown that by embedding the QM molecules in an electrostatic field of atomic point charges representing the other fragments, the expansion can be suitably truncated at the dimer level.

This fragmentation scheme can be exploited in the FMO-MS-RMD approach[1] to provide a reactive force field, as in the MS-EVB force field. This force field is derived from a linear combination of multiple states,

$$|\Psi_{\mathrm{tot}}\rangle = \sum_{A}^{N_{\mathrm{states}}} c_A |\Psi_A\rangle \qquad (2)$$

where $|\Psi_A\rangle$ is the Ath fragmentation state and c_A is the normalized coefficient of state A. Each of these states represents a different bonding topology as shown in Figure 1 and together they form a basis of expansion for the complete

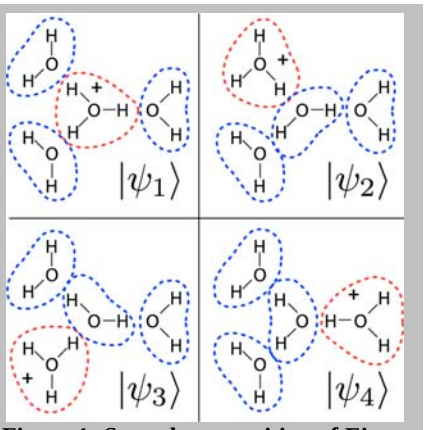

Figure 1: State decomposition of Eigen cation in FMO-MS-RMD method.

reactive molecular system $|\Psi_{tot}\rangle$, which can be evaluated on-the-fly during a molecular dynamics simulation. Typically, in MS-EVB these states are determined through *a priori* empirical fitting of classical molecular dynamics data to a subset of QM data points. This fitting procedure can be extremely laborious and can result in the lack of certain fundamental physical properties, such as charge-transfer, polarization, and other many-body effects. Additionally, the procedure may have limited transferability to other molecular systems.

The ability of QM fragmentation approaches to both efficiently and accurately evaluate large molecular systems makes them extremely useful for any type of MD simulation. Moreover, because the MS-EVB force field already introduces a level of fragmentation to the individual states, the fragmentation approaches are even more appropriate.

In FMO-MS-RMD the matrix elements of the model Hamiltonian, where the diagonal elements are given by H_{AA}, are simply the fragmented QM energies, shown in Eq. 1, and the off-diagonal coupling terms, H_{AB}, are determined empirically, but only have a small effect on the overall matrix. The FMO-MS-RMD method has been implemented using three different electronic structure packages, Q-Chem,[5] NWChem,[6] and GAMESS,[7] thus showcasing the method's overall flexibility. Initial proof of concept work has been carried out on small protonated water clusters[1] to good effect at the MP2/cc-pVDZ level of theory with noniterative FMO calculations, but the approach has also now been extended to condensed phase systems.

One such example of a condensed phase system is protonated liquid water.[8] In order to treat this type of system, the fragmentation equation should be reformulated to determine the unit-cell energy of a molecular system using periodic boundary conditions, such that

$$E_{\text{cell}} = \sum_{I} E_{I(\mathbf{0})} + \frac{1}{2}\sum_{\mathbf{n}}\sum_{I,J}{}' \left\{ E_{I(\mathbf{0})J(\mathbf{n})} - E_I(\mathbf{0}) - E_J(\mathbf{n}) \right\} + E_{\text{LR}} \qquad (3),$$

where **n** is a three-integer index of a unit cell, $E_{J(\mathbf{n})}$ is the QM energy of the *J*th fragment in the nth unit cell, $E_{I(\mathbf{0})J(\mathbf{0})}$ represents the QM energy of the dimer consisting of the *I*th molecule in the **0**th unit cell and the *J*th molecule in the nth unit cell. The prime in the summation avoids counting the $E_{I(\mathbf{0})I(\mathbf{0})}$ term and the E_{LR} refer to some long-range electrostatic contribution to the energy. The main obstacle in this type of formulation is the massive number of monomers and dimers that need to be evaluated. However, since all of the fragments are separable, the unit-cell energy equation becomes trivially parallelizable, making for efficient implementation on large supercomputers.

The combination of a fast and highly parallel FMO-MS-RMD simulation code with large-scale computing resources will enable the efficient computer simulation of large-scale reactive condensed phase systems at an unmatched level of accuracy. This procedure can also be used to check to the accuracy of the more empirical MS-EVB approach and systematically guide the improvements of such highly efficient reactive MD methods.

References (Voth)

1. Lange, A. W.; Voth, G. A., Multi-state Approach to Chemical Reactivity in Fragment Based Quantum Chemistry Calculations. *J. Chem. Theory Comput.* **2013,** *9* (9), 4018–4025.
2. Gordon, M. S.; Fedorov, D. G.; Pruitt, S. R.; Slipchenko, L. V., Fragmentation Methods: A Route to Accurate Calculations on Large Systems. *Chem. Rev.* **2012,** *112* (1), 632-672.
3. Knight, C.; Lindberg, G. E.; Voth, G. A., Multiscale Reactive Molecular Dynamics. *J. Chem. Phys.* **2012,** *137* (22), 22A525-22A525-11.
4. Allen, M. P.; Tildesley, D. J., *Computer Simulation of Liquids*. Oxford University Press, USA: **1989**.
5. Shao, Y.; Molnar, L. F.; Jung, Y.; Kussmann, J.; Ochsenfeld, C.; Brown, S. T.; Gilbert, A. T. B.; Slipchenko, L. V.; Levchenko, S. V.; O Neill, D. P.; DiStasio Jr, R. A.; Lochan, R. C.; Wang, T.; Beran, G. J. O.; Besley, N. A.; Herbert, J. M.; Yeh Lin, C.; Van Voorhis, T.; Hung Chien, S.; Sodt, A.; Steele, R. P.; Rassolov, V. A.; Maslen, P. E.; Korambath, P. P.; Adamson, R. D.; Austin, B.; Baker, J.; Byrd, E. F. C.; Dachsel, H.; Doerksen, R. J.; Dreuw, A.; Dunietz, B. D.; Dutoi, A. D.; Furlani, T. R.; Gwaltney, S. R.; Heyden, A.; Hirata, S.; Hsu, C.-P.; Kedziora, G.; Khalliulin, R. Z.; Klunzinger, P.; Lee, A. M.; Lee, M. S.; Liang, W.; Lotan, I.; Nair, N.; Peters, B.; Proynov, E. I.; Pieniazek, P. A.; Min Rhee, Y.; Ritchie, J.; Rosta, E.; David Sherrill, C.; Simmonett, A. C.; Subotnik, J. E.; Lee Woodcock III, H.; Zhang, W.; Bell, A. T.; Chakraborty, A. K.; Chipman, D. M.; Keil, F. J.; Warshel, A.; Hehre, W. J.; Schaefer III, H. F.; Kong, J.; Krylov, A. I.; Gill, P. M. W.; Head-Gordon, M., Advances in Methods and Algorithms in a Modern Quantum Chemistry Program Package. *Phys. Chem. Chem. Phys.* **2006,** *8* (27), 3172-3191.
6. Valiev, M.; Bylaska, E. J.; Govind, N.; Kowalski, K.; Straatsma, T. P.; Van Dam, H. J. J.; Wang, D.; Nieplocha, J.; Apra, E.; Windus, T. L.; de Jong, W. A., NWChem: A Comprehensive and Scalable Open-source Solution for Large Scale Molecular Simulations. *Comput. Phys. Commun.* **2010,** *181* (9), 1477-1489.
7. Schmidt, M. W.; Baldridge, K. K.; Boatz, J. A.; Elbert, S. T.; Gordon, M. S.; Jensen, J. H.; Koseki, S.; Matsunaga, N.; Nguyen, K. A.; Su, S.; Windus, T. L.; Dupuis, M.; Montgomery, J. A., General Atomic and Molecular Electronic Structure System. *J. Comput. Chem.* **1993,** *14* (11), 1347-1363.
8. Schmitt, U. W.; Voth, G. A., The Computer Simulation of Proton Transport in Water. *J. Chem. Phys.* **1999,** *111* (20), 9361-9381.

Publications acknowledging AFOSR support during the last three years (Voth):

- P. Yang, G. A. Voth, D. Xiao, J. L. G. Hines, R. A. Bartsch, E. L. Quitevis, Nanostructural organization in carbon disulfide/ionic liquid mixtures: Molecular dynamics simulations and optical Kerr effect spectroscopy. *J. Chem. Phys.,* **2011**, 135, 034502-12.

- F. Bardak, D. Xiao, L. G. Hines, P. Son, R. A. Bartsch, E. L. Quitevis, P. Yang, G. A. Voth, Nanostructural Organization in Acetonitrile/Ionic Liquid Mixtures: Molecular Dynamics Simulations and Optical Kerr Effect Spectroscopy. *Chem. Phys. Chem.,* **2012**, 13, 1687-1700.

- E. L. Quitevis, F. Bardak, D. Xiao, L. G. Hines, P. Son, R. A. Bartsch, P. Yang, G. A. Voth, Spectroscopy and Molecular Dynamics Simulations of Nonpolar and Polar Molecules in Ionic Liquids. *In Ionic Liquids: Science and Applications, American Chemical Society,* **2012**; Vol. 1117, pp 271-287.

- I. Sumner, G. A. Voth, Proton Transport Pathways in [NiFe]-Hydrogenase. *J. Phys. Chem. B*, **2012**, 116, 2917-2926.

- G. Saielli, G. A. Voth, Y. Wang, Diffusion Mechanisms in Smectic Ionic Liquid Crystals: Insights from Coarse-grained MD Simulations. *Soft Matter,* **2013**, 9, 5716–5725.

- M. McCullagh, G. A. Voth, Unraveling the Role of the Protein Environment for [FeFe]-Hydrogenase: A New Application of Coarse-graining. *J. Phys. Chem. B*, **2013**, 117, 4062-4071.

- Lange, A. W.; Voth, G. A., Multi-state Approach to Chemical Reactivity in Fragment Based Quantum Chemistry Calculations. *J. Chem. Theory Comput.* **2013,** *9* (9), 4018–4025.

Subtask III
Structure and Dynamics at Buried Interfaces in Colloids and Ionic Liquids

Hai-Lung Dai – Department of Chemistry, Temple University

Following the resolution of several problems fundamental to the understanding of Second Harmonic Light Scattering from nanometer to micron size particles, this approach has been used to effectively characterize the surface of metallic nanoparticles in colloids and at the interface between room temperature ionic liquids and an electrode.

It is shown for the first time that Second Harmonic Generation from the surface of metallic nanoparticles can be detected, and through monitoring the response of the second harmonic light to the change of the colloidal conditions, the mechanism and rates of reactions occurring at the nanoparticle surface can be determined. During this research a method was found to vastly increase the fluorescence quantum efficiency of metallic nanoparticles – a discovery that has major implications for the use of metallic quantum dots in sensor technology and biomedical imaging.

At the interface between Room Temperature Ionic Liquids and the electrode, by measuring the Second Harmonic response to the applied voltage, it is discovered that there is an electric field induced orientation in the structure of the interfacial layer of the ionic liquid. In addition, it is shown that SHG can be used to characterize the plasmonic structure of nanoparticle arrays, both materials with unique nonlinear optical properties.

1. Reactions and Adsorption of Thiols at the Surface of Silver Nanoparticles probed by SHG

Even though nanoparticles have dimensions much smaller than the optical wavelength and shapes commonly with inversion symmetry, it was shown here that Second Harmonic Generation (SHG) can be detected from the surface layer of metallic nanoparticles, in this case 40 nm radius Ag particles. The figure on the right shows the light scattered from a Ag nanoparticle colloid following irradiation with 800 nm light. The light is detected at an angle away from the propagation direction of the fundamental beam - from particle size studies it is determined at which angle to look for the maximum of the scattered SH light depending on the size as well as the materials. The scattered light consists of two parts, both from the Ag particles: The peak at 400 nm is assigned to SHG. The much weaker and broader band at longer wavelengths is from two-photon excitation induced luminescence.

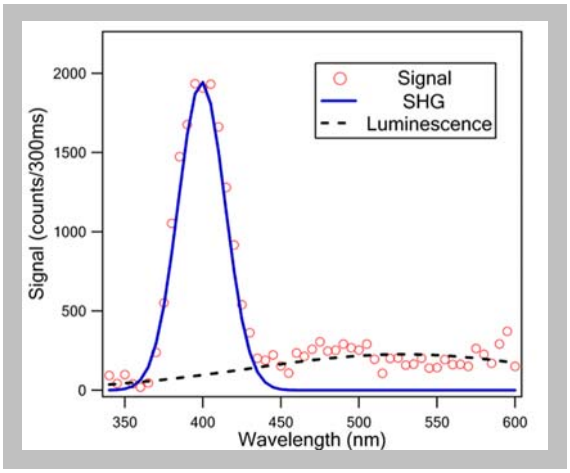

The origin of the SH intensity is confirmed

based on its response to the addition of thiol molecules that are known to form strong S-Ag bonds. Substantial (70%) decrease of SHG upon addition of thiol molecules to the Ag particle surface was observed. Apparently chemical bonding at the surface localizes the Ag electrons that are responsible for the nonlinear polarizabilty and reduces the nonlinear susceptibility. The surface generated portion of the SH intensity can thus be used for probing properties and processes at the nanoparticle surface.

Through analyzing the concentration dependent SH intensity decay, it is possible to determine the free energy, of adsorption of 1,2-benzenedithiol onto Ag nanoparticle as no larger than -8.8 kcal/mol, i.e. $|\Delta G| \geq 8.8$ kcal/mol. The decay in the time-resolved SH intensity detected from the surface of the Ag nanoparticles was found to be temperature dependent. From the adsorption constants determined at three temperatures 303, 293 and 284 K from the SHG measurements, the activation energy barrier for the adsorption of 1,2-benzenedithiol onto the surface of silver nanoparticles in aqueous colloids was determined as (8.4±0.3) *kcal/mol*. This energy barrier is too large to be associated with any physical processes such as diffusion and physical adsorption, and the result is attributed to the formation of the transition state during the bonding reaction.

2. Dramatic Enhancement of Ag Particle Luminescence Induced by Thiol Adsorption

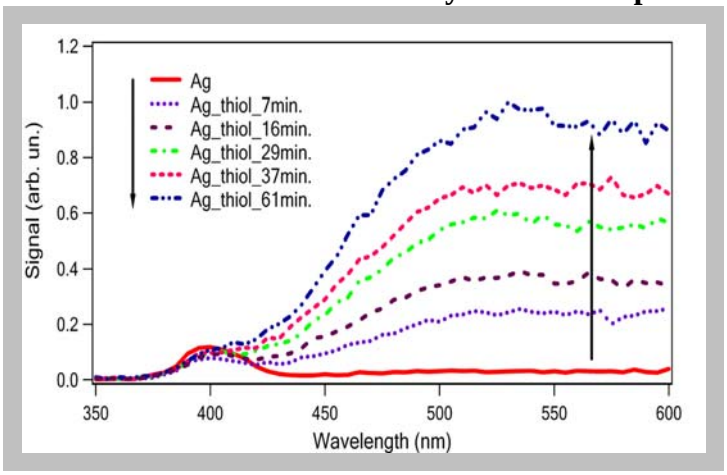

While thiol-metal bonding causes a decrease of the hyper-polarizability of the metal surface, surface bonding also affects light induced fluorescence of the metallic nanoparticles. It was observed that while SHG from the silver colloid decreases upon the addition of ethanethiol, the two-photon luminescence (TPL) on the contrary is greatly enhanced (by as much as 300 times). Both phenomena are shown to arise from the same structural change, the formation of strong S-Ag bonds, at the surface.

The figure above shows that following the addition of a fixed amount of ethanethiol, the TPL signal continues to increase, by more than two orders of magnitude. Significantly and interestingly, the TPL increase occurs on a time scale (tenths of minutes) much slower than the SHG decrease (tens of seconds, see Section 1).

The enhancement of the luminescence signal results from elimination of defects (or dangling bonds) on the silver particle surface by thiol adsorption. The surface defects or dangling bonds are known to trap excited electrons and reduce the luminescence efficiency of nanoparticles and quantum dots. The effect of thiol adsorption on the enhancement of the luminescence signal can be quantitatively accounted for by the same adsorption model that is

used to describe the SHG decrease. The time lag of the TPL increase with respect to the SHG decrease can be explained by the fact that the effective quenching cross section of a defect is much larger than the physical area the defect occupies. In this case, a substantial amount of the defects has to be eliminated before the effect on TPL becomes appreciable.

3. Structure and Dynamics at the Interfaces of Room Temperature Ionic Liquids

Here SHG is also used for studying the surfaces of the RTIL and the interfaces between the Room Temperature Ionic Liquids and the electrodes. The small amount of molecules at the interface can generate a detectable nonlinear signal while the molecules in the bulk with much larger quantities make little contribution because of the isotropic orientation in the liquid solution.

The presence of an applied external potential is expected to induce a response in the charge distribution in a high resistance electrolyte at the electrolyte-electrode interface: the ions with the opposite charge to the electrode polarity would have a higher concentration in the layer immediately next to the electrode surface followed by the counter ions in the next layer. This ionic double layer would generate an electric field in the opposite direction to the applied field which subsequently screens the applied field. The result is a tremendous drop of the electrical potential over the double layer, producing a giant electric field on the magnitude of V/nm. This giant electric field may exert a unique influence on the structure of the RTIL surface. The cations of the RTIL with chain-like molecular structure usually have large dipole moment, they may orient in the direction along the applied field.

In general, because the 2nd order nonlinear susceptibility of RTIL ions is small, SHG from the RTIL can be detected only when the orientation of the ions is not isotropic. It is possible that an external electric field may induce such orientation order and/or charge separation to cause asymmetry and facilitate dipole-allowed SHG. This external electric-field induced nonlinear phenomenon would depend on the electric field strength. Since it is likely that this field will be screened by the charge-separated bilayer at the interfacial region, and the applied potential will rapidly decrease after the bilayer into the bulk, the SH signal generated will be from only the molecular ions with orientation order at the interface. The SH signal can thus be used to monitor the field-induced structural change in the fast potential-drop region at the RTIL|electrode interface.

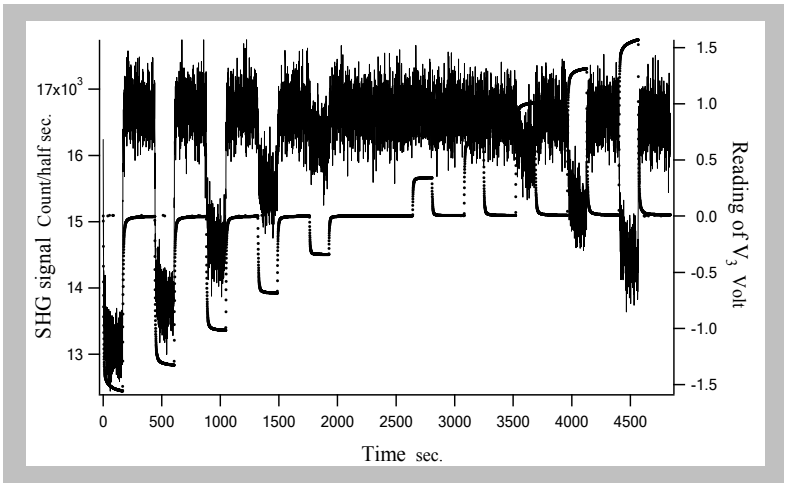

Here it is shown that there is measurable SH signal from the

interface and that it responds to the applied potential. A potential-dependent SH signal from the front ITO|RTIL interface is shown in the Figure. The RTIL used in this experiment is $[C_{12}PPY][C_2C_2N]$. The ITO film serves as the electrode for applying the potential. The SH signal displays substantial change in response to the applied potential: In general the SH intensity decreases when the external potential is applied. The SH intensity recovers instantly when the potential is removed. The overall behavior of the SH intensity as a function of the applied voltage is shown here. The change of the SH intensity with the applied potential appears as a downward, almost symmetric parabolic shape with the maxima located at ~ 0.5 V.

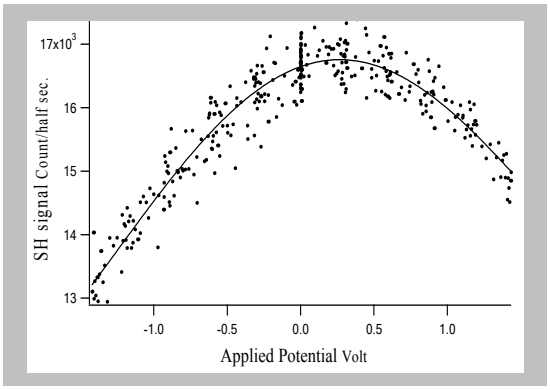

The method can quantitatively characterize the interfacial SHG response to the applied electric potential. These observations clearly indicate significant and interesting physical and chemical effects induced by the giant electric field caused by the applied potential at the interfaces of RTIL thin films.

4. Nonlinear Optical Probe of Deep-UV Plasmonics in Aluminum Nanoparticle Arrays

In a collaboration with a synthetic group in Italy the Dai group has shown that small aluminum nanoparticles have the potential to exhibit localized surface plasmon resonances in the deep ultraviolet region of the electromagnetic spectrum, but technical and scientific challenges make it difficult to attain this limit. The fabrication of arrays of Al/Al2O3 core/shell nanoparticles is reported, with a metallic-core diameter between 12 nm and 25 nm that display sharp plasmonic resonances at very high energies, up to 5.8 eV (down to $\lambda = 215$ nm). The arrays were fabricated by means of a straightforward self-organization approach. The experimental spectra were compared with theoretical calculations that allow the correlation of each feature to the corresponding plasmon modes.

Publications acknowledging AFOSR support during the last three years (Dai):

- W. Gan, G. Gonella, M. Zhang and H.-L. Dai, Reactions and Adsorption at the Surface of Silver Nanoparticles probed by Second Harmonic Generation, *J. Chem. Phys.*, **2011**, 134, 041104-6.

- W. Gan, B. Xu and H.-L. Dai, Activation of Thiols at a Ag Nanoparticle Surface, *Angewandte Chemie Int. Ed.*, **2011**, 50, 6622-25 (designated as Very Important Paper).

- G. Gonella and H.-L. Dai, Determination of adsorption geometry on spherical particles from nonlinear Mie theory analysis of surface second harmonic generation , *Phys. Rev. B [Rapid Communication]*, **2011**, 84, 121402(R)/1-5.

- L. A. Burke, G. Gonella, F. Heirtzler, H.-L. Dai, S. Jones, J. Zubieta, A. J. Roche, A self-assembled, metallo-organic supramolecular frequency doubler, *Chem. Commun.*, **2012**, 48, 1000-2.

- S. Roke and G. Gonella, Nonlinear light scattering and spectroscopy of particles and droplets in liquids, *Annu. Rev. Phys. Chem.,* **2012**, 63, 143748.

- G. Gonella, W. Gan, B. Xu, H.-L. Dai, Effect of Composition, Morphology and Susceptibility on Nonlinear Light Scattering from Metallic and Dielectric Nanoparticles, *J. Phys. Chem. Lett.*, **2012**, 3, 2877–81.

- G. Maidecchi, G. Gonella, R. Moroni, L. Anghinolfi, A. Giglia, S. Nannarone, L. Mattera, H.-L. Dai, M. Canepa, F. Bisio, Deep Ultraviolet Plasmon Resonance in Aluminum Nanoparticle Arrays, *ACS Nano*, **2013**, 7, 5834-5841.

- G. Maidecchi, G. Gonella, R. Proietti Zaccaria, R. Moroni, L. Anghinolfi, A.Giglia, S. Nannarone, L. Mattera, Hai-Lung Dai, M. Canepa and F. Bisio, Deep Ultraviolet plasmonics in Aluminum Nanoparticle arrays, *Elettra*, **2012/2013**, 38-9.

- G. Gonella and H.-L. Dai, Second Harmonic Light Scattering from the Surface of Colloidal Objects: Theory and Applications, *Langmuir*, **2014**, 30, 2588-99, (invited feature article).